

ARTICLE



<https://doi.org/10.1038/s42005-020-00496-x>

OPEN

Weighing picogram aerosol droplets with an optical balance

Oliver Reich¹, Grégory David¹  , Kıvanç Esat¹ & Ruth Signorell¹ 

Optical traps are used to isolate and manipulate small objects in air and liquids, enabling the thorough characterization of their properties in situ. However, no broadly applicable technique for mass measurements of optically trapped objects is currently available. Here we propose an optical balance for mass measurements of optically trapped aerosol particles. By analyzing light-induced harmonic oscillations of a particle, its mass is determined non-destructively and with high accuracy on a time scale of seconds. Its performance is demonstrated for aqueous salt droplets, where masses as low as 4 pg (4×10^{-15} kg) have been measured with an accuracy of ~ 100 fg. The balance is straightforward to implement and broadly applicable.

¹Department of Chemistry and Applied Biosciences, ETH Zurich, Vladimir-Prelog-Weg 2, CH-8093 Zurich, Switzerland. email: gregory.david@phys.chem.ethz.ch; rsignorell@ethz.ch

Optical traps are widely used to isolate small objects in the liquid phase, in the gas phase and in vacuum. The importance such traps have gained has been recognized by the 2018 Nobel prize in Physics awarded to Arthur Ashkin for the invention of optical tweezers and their applications¹. Optical traps serve to manipulate small objects in different environments (liquid, gas, vacuum), and for ultrasensitive measurements of forces and torques^{2–12}. With many applications in the liquid phase related to biological systems^{13,14}, such as proteins or living cells, they play a key role in developing and shaping the fields of biophysics and biology^{4,13,14}. Optical trapping has also been realized in low-pressure environments, e.g., for the quantification of the Brownian motion¹⁵ or to study fast particle rotations^{2,16} and the momentum transfer from light to trapped particles¹⁷. In the gas phase, optical traps enable the characterization and manipulation of single isolated aerosol particles and droplets in the submicrometer-size and micrometer-size range with attoliter to picoliter volumes^{4,18–20}. Studies typically focus on properties such as size, shape, refractive index, chemical composition, viscosity, and surface tension^{21–25} with the goal to improve our understanding of aerosol processes, such as phase transitions²⁶, diffusion²⁴, evaporation^{20,27,28}, coagulation²⁹, photochemistry³⁰, reactions with gases or radicals^{20,31,32}, and hygroscopic growth^{20,27}.

Despite the fact that the mass is a key quantity, a broadly applicable method for the determination of the mass of optically trapped aerosol droplets and particles has so far not been demonstrated. Currently, the electrodynamic balance (EDB)^{33–37} is the reference technique to determine the mass of single particles isolated in air. EDBs provide non-destructive, high-accuracy (in the percent range) mass measurements of particles, but they require prior charging of the particles and mass calibration. They usually provide mass measurements for larger particles with radii ranging from a few to many micrometers, not accessing the submicron range. Submicron-sized droplets and particles are particularly relevant in many atmospheric processes, such as scattering and absorption of sunlight^{38,39} or size-dependent enhanced kinetics^{22,40,41}. Mass measurements of aerosol particles in optical traps are limited to the special case of photophoretic traps^{42,43}. They require the particle to absorb the light of the trapping laser, which heats the particle. In addition to the size limitation to particles of at least a few⁴³ to a few ten⁴² micrometers in radius, the heating substantially restricts the applicability of these traps to absorbing, non-volatile particles, basically excluding all volatile and semi-volatile particles, in particular also aqueous droplets. With a typical accuracy of 15%^{42,43}, they do currently not reach the accuracy of EDBs.

This study reports an optical balance for the non-destructive mass determination of optically trapped aerosol droplets and particles with sizes down into the submicron range (lower picogram range). Using modulated counter-propagating optical tweezers, the mass of an aqueous NaCl droplet is determined by inducing harmonic oscillations and analyzing the resulting dynamics. The mass is obtained with high accuracy (less than 2%) at different relative humidities (RH), and the hygroscopic mass growth of the droplet is quantified. The optical balance is straightforward to implement, does not require particle charging, and can even be used without prior mass calibration, which makes it broadly applicable for many studies in aerosol science, or other scientific fields which use optical trapping.

Results

Principle of mass measurement. Dual beam traps are widely used to trap particles^{15,44–49}. Fig. 1a shows a sketch of the counter-propagating optical tweezers^{30,50} (CPT) used for

trapping single aqueous NaCl droplets at ambient pressure (see “Methods” section for droplet generation and control of the relative humidity). Light from a continuous 532 nm laser (Opus 532, Laser Quantum, typical power ≈ 1 W) passes through a Faraday isolator (Thorlabs, IO-5-532-HP) to avoid back reflections returning to the laser. A half-wave plate is used to orient the polarization of the laser horizontally before the electro-optic modulator (EOM, Conoptics, 350-50-01-RP), which is used to control the polarization of the laser beam. The laser beam is then expanded four times by a two-lens telescope (focal lengths of 50 and 200 mm). A polarization beam-splitter cube (PBC) splits the incident laser beam into two counter propagating beams. The beams are focused with two aspherical lenses (CVI, BFPL-25.4-50.0-UV, 56.6 mm focal length at 532 nm) in the center of a trapping cell, where a single aerosol droplet is immobilized (brown dot). One half-wave plate is used in each trapping beam to align the polarization of the two beams parallel to each other. A path length difference of approximately 50 cm between the two trapping beams is used on purpose to avoid interference between the two beams (the coherence length of the laser is 7 mm). The optical forces are controlled via the power ratio of the two counter-propagating beams with the EOM. By modulating the power ratio of the two beams sinusoidally in time, a harmonic oscillation of the particle is induced along the beam propagation direction (Fig. 1b). The driven harmonic oscillation of the droplet is described by the following equation of motion (see “Methods” section):

$$\ddot{z} + 2\pi\Gamma_0\dot{z} + 4\pi^2f_0^2z = 4\pi^2f_0^2Z_0\sin(2\pi ft) \quad (1)$$

where z is the position of the droplet along the axis of the laser beams, f_0 is the natural frequency of the oscillator and Γ_0 is its damping rate. The modulation amplitude Z_0 (amplitude corresponding to the position change of the minimum of the trapping potential) and the modulation frequency f of the oscillation are controlled by the modulated voltage applied to the EOM. Equation (1) is solved by

$$z(t) = a\sin(2\pi ft - \varphi) \quad (2)$$

where a is the amplitude of the droplet’s oscillation and φ is its phase. The droplet position is measured by a position sensitive photodiode (PSP) connected to a lock-in amplifier. During the harmonic oscillation of the droplet, the lock-in amplifier directly measures a and φ . For the data analysis, we prefer φ over a because of correlation issues with the latter (see “Discussion” section). A sweep of the modulation frequency provides $\varphi(f)$, from which f_0 and Γ_0 are retrieved by fitting the experimental data to Eq. (3):

$$\tan(\varphi) = \frac{\Gamma_0 f}{f_0^2 - f^2} \quad (3)$$

The absolute mass m of the droplet is then determined from Eq. (4):

$$m = \frac{3R\mu}{C_c\Gamma_0} \quad (4)$$

where R is the particle radius, μ is the dynamic viscosity of the surrounding fluid (nitrogen in our case) and C_c is Cunningham’s correction factor⁵¹. Equation (4) shows that an additional measurement of R is sufficient to calculate the mass of the droplet from Γ_0 . We use broad-band light scattering (BLS)^{30,50} to determine R (Fig. 1b, “Methods” section and Supplementary Note 1). With our optical balance, m can be retrieved without mass calibration, in contrast to mass measurements with EDBs which require calibration.

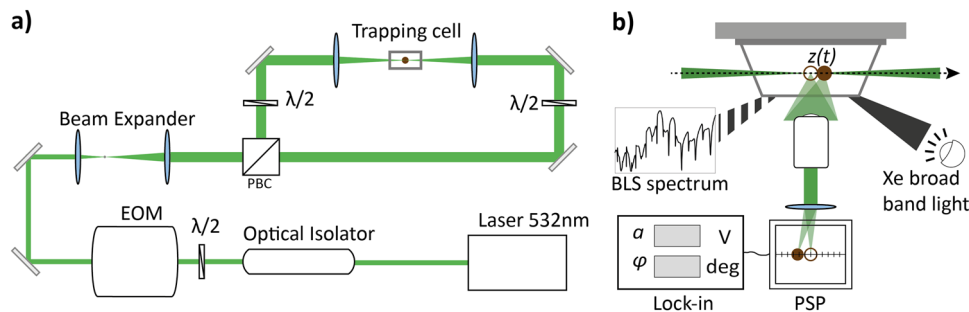


Fig. 1 Sketches of the experimental setup. **a** Layout of the counter-propagating optical tweezers. A half-wave plate ($\lambda/2$) is used to adjust the polarization at 45° to the crystal axes of the electro-optic modulator (EOM). The laser beam is split at the polarization beam splitter cube (PBC) according to the polarization of the light set by the EOM. The particle (brown dot) is trapped in the cell between the foci of the two trapping beams. **b** Determination of the droplet's shift in position $z(t)$ along the axis of the trapping beams (dashed arrow) and of its radius R . A position sensitive photodiode (PSP) tracks $z(t)$ by measurements of the light scattered by the droplet. When the droplet moves from the position of the brown empty circle to the full circle, the position of the collected scattered light on the PSP changes accordingly. During the modulation of the trap the amplitude a and phase φ of the particle oscillation are measured with a lock-in amplifier. The broad-band light scattering spectra (BLS) are obtained by illuminating the particle with a broad-band Xe lamp (filled triangular beam), and recording the light elastically scattered by the droplet as a function of the wavelength (hatched black triangular beam).

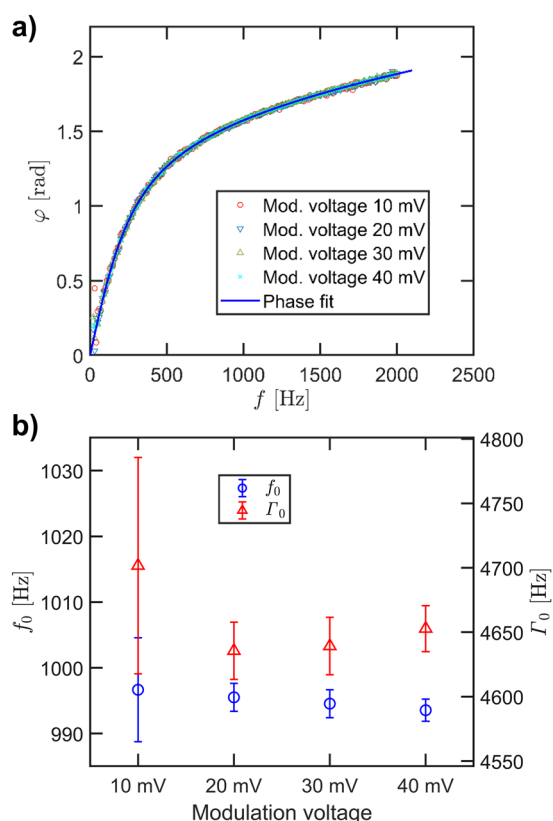


Fig. 2 Phase (φ) measurements and retrieved f_0 and Γ_0 for different modulation voltages. **a** φ as a function of the frequency f for a trapped aqueous NaCl droplet at a relative humidity of 68% for four different electro-optic modulator voltages of 10, 20, 30, and 40 mV (see symbols in the legend). The data points for the different voltages virtually coincide with each other. The same holds for the fits. For clarity, we only show one of the fitted $\varphi(f)$ curves (solid blue trace). **b** Natural frequency f_0 (blue circles) and damping rate Γ_0 (red triangles) as a function of the modulation voltage, retrieved from fits to the phase measurements in panel **a**. The error bars indicate the 68% confidence interval of the fits.

Harmonicity of the droplet oscillation. The harmonicity of the trapping potential and the induced particle oscillation is verified by the results presented in Fig. 2. Fig. 2a shows an example measurement of φ as a function of f for a trapped aqueous NaCl

droplet at an RH of 68% for four different EOM modulation voltages between 10 mV to 40 mV. The latter correspond to values for the amplitudes Z_0 between $\sim 10 \mu\text{m}$ and $40 \mu\text{m}$. The measured $\varphi(f)$ are essentially identical for the four different modulation voltages. Fig. 2b illustrates that the values for Γ_0 (right ordinate) and f_0 (left ordinate) retrieved from the data in panel a using Eq. (3) agree within their uncertainty for the four different modulation voltages. These uncertainties lie below 0.5% for the measurements with the 20, 30, and 40 mV modulation voltage. For the measurement at 10 mV modulation voltage, the uncertainties of Γ_0 and f_0 are slightly larger (2% and 1%, respectively). This is due to the smaller Z_0 resulting in a lower signal-to-noise ratio for $\varphi(f)$. From Fig. 2 it is clear that $\varphi(f)$, Γ_0 and f_0 are virtually independent of Z_0 (i.e., the modulation voltage), which demonstrates that the harmonic approximation provides a very good description of the trapping potential and the induced particle oscillation.

In the rare case when the droplet size and the wavelength of the trapping laser precisely match a resonance condition, so that a Mie resonance (also called morphology dependent resonance or whispering gallery mode) is excited in the droplet⁵², its dynamics does no longer follow a harmonic oscillation (see Supplementary Note 2 and Supplementary Fig. 2). Fortunately, Mie resonances are limited to very specific combinations of particle size and wavelength so that they do not pose any practical limitation to the mass measurement. If a resonance is encountered, a minute (sub-percent) change of the relative humidity is enough to restore the harmonic oscillation of the particle.

Mass measurement and related quantities. Fig. 3a shows the mass m (red triangles) retrieved for aqueous NaCl droplets with the same NaCl content, but varying water content given by the RH. The chosen range of RH covers both supersaturated and undersaturated concentrations (the critical RH of NaCl is $75.3 \pm 0.3\%$ ⁵³). m is retrieved from Γ_0 and R using Eq. (4). The accuracy of m is limited by systematic errors and random errors. The systematic error mainly arises from uncertainties of the spot size of the scattered light on the PSP, and is estimated to lie below 3.5% of the droplet mass (see “Methods” section, Supplementary Note 3 and Supplementary Fig. 3). We further estimate the random error to be less than 2–3% of the droplet mass. With a maximum systematic error of 3.5% and a maximum random error of 2–3%, we specify a maximum total error of 5.5–6.5%. For the specific data in Fig. 3a—which cover droplet sizes in the micron range—we determined a systematic error of 2% (see

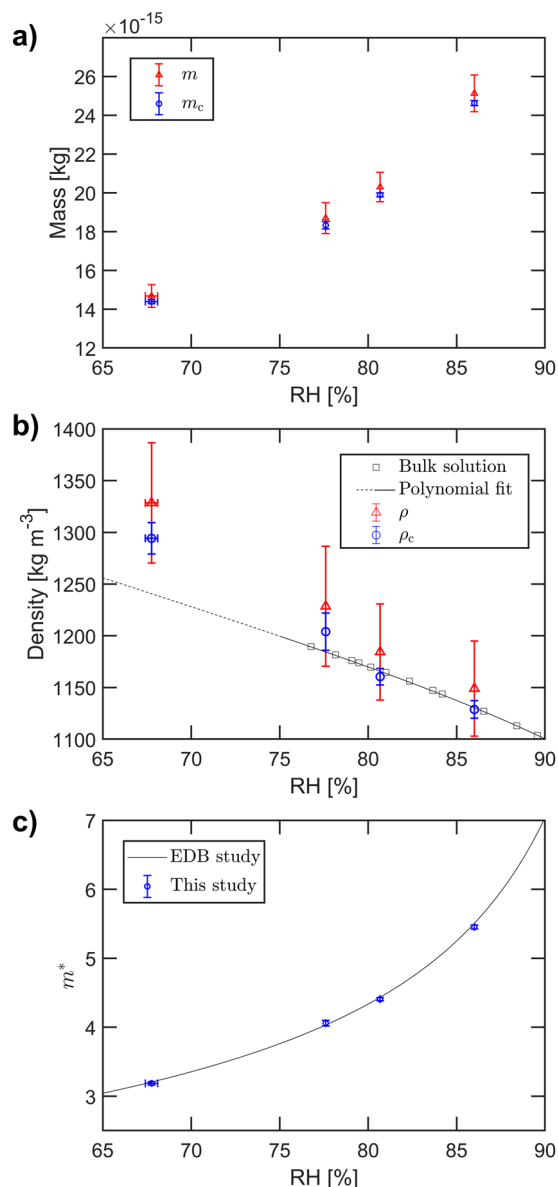


Fig. 3 Mass, density, and mass growth factor of aqueous NaCl droplets.

a Droplet mass before (m , red triangles) and after calibration (m_c , blue circles) as a function of relative humidity (RH). **b** Droplet densities before (ρ , red triangles) and after calibration (ρ_c , blue circles) as a function of RH. The density of the bulk solution is indicated by black squares^{54,66}. The black line represents bulk densities with an extrapolation into the supersaturation region (dashed line)³⁵. The discrepancy between the extrapolation and our measurement is addressed in the “Discussion” Section. **c** Mass growth factors m^* from this study (blue circles) and from an earlier study with an electrodynamic balance (EDB) (black line)³⁵ as a function of RH. Horizontal error bars indicate the RH variation during the measurements. Vertical error bars for the uncalibrated m and ρ are the sum of the systematic error and the random error, while the error bar for the calibrated m_c and ρ_c and for m^* indicate the random error only.

below) and random errors between 0.5 and 1.9% (Table 1). The maximum random error for submicron droplets ($R \sim 800$ nm, m of few picograms; not listed in Table 1) is somewhat larger around 3%. A maximum total error of 5.5–6.5% represents a high accuracy, in particular when one considers that this is achieved for very low absolute droplet masses in the lower picogram range without any mass calibration.

Access to the lower picogram mass range combined with this level of accuracy already provides satisfactory results for many applications. Mass calibration with a suitable reference allows us to correct for the systematic error and thus to improve the accuracy even further to the level of the random error of less than 2–3%. The calibration can be performed by comparing the measured density of the aqueous NaCl droplets (from R and m) to the density of corresponding bulk solutions⁵⁴ (Fig. 3b). We determine a constant calibration factor $C = 0.98$ for the density ($\rho_c = C \cdot \rho$), and use the same factor for mass calibration ($m_c = C \cdot m$). m_c and ρ_c denote the mass and the density, respectively, after calibration (Fig. 3a and b and Table 1). A constant mass calibration factor of 0.98 indicates a systematic bias of 2%, and corrects the systematic error mentioned above. (See the “Discussion” section for a further discussion of Fig. 3b).

In addition to the droplet mass and density, our optical balance also allows us to retrieve hygroscopic mass and size growth factors. The mass growth factor is defined as $m^*(RH) = m(RH)/m_{NaCl}$, where $m(RH)$ is the droplet mass at a given RH and m_{NaCl} is the NaCl mass in the solution droplet (see “Methods” section). Note that $m^*(RH)$ does not depend on the calibration. Fig. 3c compares m^* from this study with results from a previous investigation with an EDB³⁵. Almost perfect agreement is observed between the two different studies, which demonstrates that mass measurements with the optical balance can easily compete with mass measurements in EDBs. The droplet size growth factor is defined as $R^*(RH) = R(RH)/R_{dry}$, where $R(RH)$ is the droplet radius at a given RH and R_{dry} is the radius of a completely dried particle (see Supplementary Note 4 for calculation of R^*). The R^* values retrieved for the data in Table 1 lie between 1.75 and 2.19 (see Supplementary Note 4 and Supplementary Fig. 4). To allow comparison with previous measurements performed with hygroscopic tandem differential mobility analyzers (HTDMA) at 90% RH, we extrapolate R^* to 90% RH (see Supplementary Note 4). The retrieved $R^*(90\%) = 2.40 \pm 0.02$ agrees within uncertainties with theoretical predictions⁵⁵ and the HTDMA measurements ($R^*(90\%) = 2.27\text{--}2.46$)⁵⁶.

Discussion

Range and accuracy of mass measurements. The optical balance permits mass measurements of aerosol particles in the picogram range, down to at least 4×10^{-15} kg. The accuracy lies at 5.5–6.5% without and at 2–3% with mass calibration. The latter corresponds to a sensitivity of $\sim 10^{-16}$ kg (100 fg) for the smallest droplet reported here. The optical balance extends particle mass measurements into the submicrometer size range, i.e., to masses that are a few orders of magnitudes lower than typical measurements in EDBs^{34,35} and photophoretic traps^{42,43}, and hence substantially broadens the range of applications (see below). It is not only the extended mass range that makes it more versatile compared with photophoretic traps and EDBs, but also the fact that the balance is neither limited to charged particles (as EDBs are) nor to non-volatile, light-absorbing solid particles (as photophoretic traps are).

The very high mass accuracy of the optical balance could only be achieved because we use the phase (φ) and not the amplitude (a) in the analysis of the droplet dynamics. The example in Fig. 4 illustrates that in certain ranges the mass cannot be determined unambiguously from $a(f)$ because Γ_0 and f_0 are strongly correlated. As a consequence, $a(f)$ can become indistinguishable for different combinations of Γ_0 and f_0 (blue full and dashed line); i.e., for different masses (in Fig. 4 for two masses that differ by a factor of 2.25). This issue does not arise for $\varphi(f)$ because f_0 is the frequency f at which $\varphi(f_0) = \pi/2$ (crosses in Fig. 4). Hence, a

Table 1 Radius (R), mass before (m) and after calibration (m_c), density after calibration (ρ_c), and mass growth factor (m^*) for micron-sized NaCl droplets at different relative humidities (RH).

RH [%]	R [μm]	m [10^{-15} kg]	m_c [10^{-15} kg]	ρ_c [$\text{kg}\cdot\text{m}^{-3}$]	m^*
67.5	1.385 ± 0.013	14.7 ± 0.59	14.39 ± 0.11	1294 ± 15	3.19 ± 0.02
77.6	1.537 ± 0.018	18.7 ± 0.79	18.33 ± 0.19	1204 ± 18	4.06 ± 0.04
80.7	1.600 ± 0.008	20.3 ± 0.76	19.90 ± 0.10	1161 ± 8	4.41 ± 0.02
86.1	1.733 ± 0.010	25.1 ± 0.95	24.62 ± 0.13	1129 ± 9	5.45 ± 0.03

The uncertainties quoted for R and m account for both systematic and random errors. Those for m_c , ρ_c , and m^* only include random errors. m_c and ρ_c are obtained with a calibration constant $C = 0.98$.

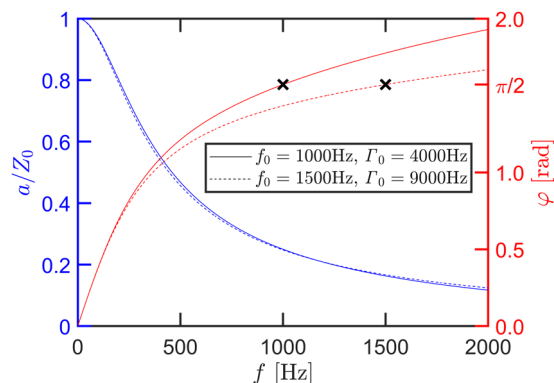


Fig. 4 Simulated phase and amplitude measurement. φ (red lines) and a (blue lines, normalized by the modulation amplitude Z_0) as a function of the frequency f for two different parameter sets f_0 and Γ_0 (dashed lines and full lines), where f_0 is the natural frequency of the particle and Γ_0 is its damping rate. The black crosses mark the points where $\varphi(f = f_0) = \pi/2$. A unique solution for the mass can only be obtained from $\varphi(f)$, but not from $a(f)$.

unique solution is obtained for the particle mass when the phase is used instead of the amplitude. The issue with $a(f)$ especially arises when the particle motion is overdamped. i.e., for smaller aerosol particles and for particles suspended in liquids.

Applications. The optical balance allows one to access properties of supersaturated solutions, which in general cannot be retrieved from bulk measurements because of precipitation. Among those properties is the density of supersaturated solutions. Comparison with bulk densities is only possible in the undersaturated regime, i. e. for aqueous NaCl solutions above the critical RH of 75.3% (Fig. 3b). Tang et al.³⁵ suggests a polynomial extrapolation for the bulk density down to RHs of $\sim 50\%$. The corresponding extrapolation (black line in Fig. 3b), however, reveals that a $\sim 4\%$ lower density is obtained at an RH = 68% using this bulk extrapolation compared with our experimental value—a difference that lies outside the experimental uncertainty of $\sim 1.2\%$ (Table 1). The origin of this discrepancy between droplet experiment and bulk extrapolation is not obvious and offers an intriguing subject for further studies.

The knowledge of hygroscopic properties of atmospheric droplets is crucial for determining their radiative forcing⁵⁷. To fully capture their effects, a comprehensive quantification of RH-dependent droplet properties (e.g., size, mass, and density) is required. An interesting phenomenon is the so far unexplained size-dependence of R^* for NaCl and sea salts droplets that was previously reported in droplet studies with HTDMAs^{56,58,59}. Depending on the instrument, HTDMA studies are limited to droplets with corresponding dry salt radii in the range

$R_{\text{dry}} \sim 100\text{--}175$ nm⁶⁰. EDBs, on the other hand, typically cover much larger particle sizes (R_{dry} of a few micrometers), so that the size range in-between remains unexplored. R^* studies with our optical balance will allow us to fill this gap (this study $R_{\text{dry}} \sim 500$ nm and larger), and to address potential size-dependent effects of R^* in this intermediate size range. Similarly, the optical balance also opens up studies of m^* in this intermediate size range. To the best of our knowledge, m^* has only been reported for supermicrometer-sized particles using EDBs.

These are only few examples of the broad applicability of our optical balance. Aerosol science is expected to be a major area of use of this method. However, we also anticipate the optical balance to be of broad interest for mass measurements of small objects in the liquid phase, such as cells and other biological samples. Many studies exist that determine the mass of objects in liquids^{61–64} and many studies apply optical trapping in the liquid phase^{3,11,12,65}, but a combination of both methods has not yet been demonstrated. The optical balance we propose solves the issue of mass determination under overdamped conditions (Fig. 4), so that it might offer a possibility to combine optical trapping applications with mass determination in the liquid phase.

Our optical balance permits mass measurements of aerosol particles with masses in the picogram range, and probably beyond, with a high accuracy of 2–3%, covering a particle size range from micrometers down to submicrometers. The implementation of the balance combines the advantage of a straightforward experimental setup with the applicability to a wide variety of particles (liquid, solid, volatile, non-volatile, charged, uncharged). Its demonstrated performance extends mass measurements of aerosol particles into regions previously inaccessible. Aerosol studies related to atmospheric and technical processes, including pharmaceutical and medical applications, will profit from this extended capability. Beyond aerosol studies, the proposed optical balance holds promise for applications in the liquid phase, enabling the combination of optical trapping and mass measurements with intriguing possibilities, e.g., for the investigation of optically trapped cells and other biological objects.

Methods

Droplet generation and relative humidity control. The particles were generated from 0.5 M aqueous NaCl solutions using a commercial atomizer (TSI 3076) with pressurized humidified nitrogen (purity 5.0). The use of humidified nitrogen ensures the delivery of liquid droplets to the trapping cell. The concentration of the trapped aqueous NaCl solution droplets is determined by the RH in the trap (and not by the concentration of the initial solution) where the trapped droplets equilibrate quickly to the surrounding RH. The RH in the cell is varied between ~ 60 and 90% by mixing dry and wet nitrogen with individually adjustable flow rates. The RH in the trapping cell is measured with a sensor (Sensirion, SHT31) placed a few millimeters away from the trapped droplets. The trapping cell is shown in Fig. 5. The cell is equipped with fused silica windows to transmit the light beams of the CPT, the BLS and the scattered light used for the position measurement. Additional apertures are used for the RH sensor and the gas flows through the cell.

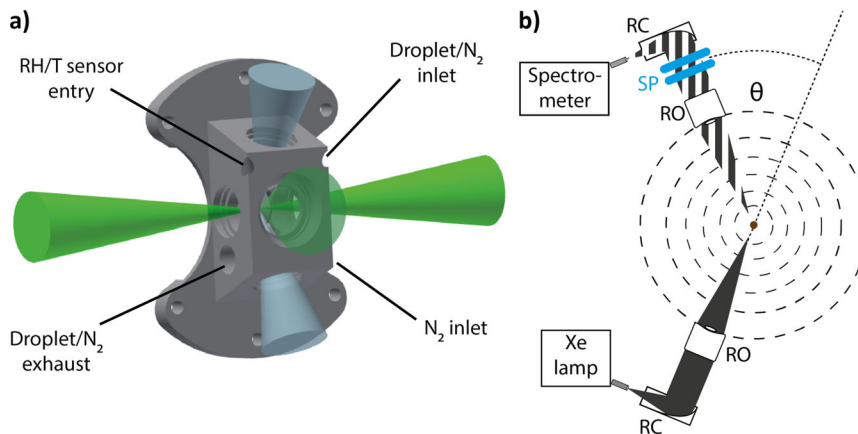


Fig. 5 Drawing of the trapping cell and sketch of the BLS optics. The trapping cell is shown in **a**. The counter-propagating tweezer beams propagate through the trapping cell as shown by the two green cones on the sides of the cell. The broad-band light scattering (BLS) emission and collection are represented by the two blue cones. The scattering light used to measure the particle position is shown by the large green cone in front of the cell. Humidified nitrogen (N_2) flow is used to control the relative humidity in the cell. The BLS optics is sketched in panel **b**. The broadband light of a Xe lamp is shone on the particle by using reflective collimators (RC) and a reflective objective (RO). The dashed circles represent the elastically scattered light. The black dashed triangle indicates the fraction of the scattered light collected by the second RO around the scattering angle θ , which is then coupled into the spectrometer using another RC. Two shortpass filters (SP) in the collection optics of the BLS attenuate the scattering of the trapping laser.

Droplet dynamics. The time dependent position $z(t)$ of the trapped droplet along the trapping axis is described by Newton's equation of motion, $m\ddot{z} = F_{\text{drag}} + F_{\text{opt}}$, where $F_{\text{opt}}(z)$ is the optical force, $F_{\text{drag}} = -\gamma\dot{z}$ is the drag force due to the surrounding fluid and γ is the drag coefficient. The droplet motion perpendicular to z is negligible in our experiments and is not considered here. Following the harmonic oscillator model, the optical potential $V_{\text{opt}}(F_{\text{opt}} = -\partial/\partial z V_{\text{opt}})$ is defined by a second order Taylor expansion $V_{\text{opt}}(z,t) = k/2(z - z_0(t))^2$, where k is the trap stiffness and $z_0(t)$ is the time dependent position of the minimum of the trapping potential during the modulation. For a sinusoidal modulation of the EOM voltage, the minimum of the trapping potential oscillates as $z_0(t) = Z_0 \sin(2\pi ft)$, where Z_0 is the amplitude and f the frequency of the oscillation. Stokes' law is used to calculate $\gamma(R) = 6\pi\mu R/C_c(R)$, where R is the radius of the droplet, μ is the dynamic viscosity of the surrounding fluid (nitrogen) and $C_c(R)$ is the size dependent Cunningham correction factor. As explained in details in ref. ⁵¹, the Cunningham correction factor accounts for the nonlinear decrease in the Stoke's drag force when the particle size approaches the molecular mean free path of the surrounding fluid. It is given by $C_c(R) = 1 + 1.26\lambda_N/R$. λ_N is the mean free path in nitrogen ($\lambda_N \approx \lambda_{\text{air}} = 68 \text{ nm}$ at 20°C). Using the quantities defined in this paragraph, $f_0 = 1/2\pi\sqrt{k/m}$ and $\Gamma_0 = \gamma/2\pi m$ in Newton's equation yields Eq. (1). Substitution of γ in the expression for Γ_0 yields Eq. (4).

Phase measurement and systematic error. $z(t)$ is measured with a commercially available PSP connected to a lock-in amplifier (Zurich Instruments, 500 kHz MFLI). The reference output of the lock-in amplifier is used to drive the EOM (ConOptics) and serves as the reference for the demodulation. During the frequency sweeps of the reference output ($f \in [0, 2] \text{ kHz}$), the raw phase is obtained directly from the demodulation of the signal of the droplet position along z by the lock-in amplifier. The signal is obtained by dividing the differential photodiode current by the total photodiode current. The measurement of the particle position is slightly delayed by the frequency-dependent impedance of the PSP and the read-out electronics. This delay as a function of modulation frequency, which has to be subtracted from the raw phase to yield $\varphi(f)$, is determined separately by monitoring the modulation of one of the trapping beams in the frequency range $[0, 5] \text{ kHz}$. The phase of this signal is equal to the delay of the PSP and readout electronics because the response time of the EOM to the applied voltage and the light propagation are much faster than the modulation periods used in this study. The PSP and its collecting optics (Fig. 1b) are mounted on a translation stage to adjust the focus of scattered light on the photosensitive area of the PSP. The focusing of the collected light on the PSP sensor affects the accuracy of the particle position tracking. It is mostly responsible for the systematic error of the mass measurement. We have quantified this effect on the accuracy of the mass measurement by repeating phase measurements for different focus sizes. This data is reported in the Supplementary Information (Supplementary Note 3 and Supplementary Fig. 3). Generally, we estimate that the maximal error in the mass measurement caused by the light focus can be up to 3.5% of the absolute droplet mass. For the current measurements, it is 2%. The light focus is not changed between measurements at different RHs, so that the same systematic error applies to all mass measurements reported here.

Random error. The random error of the mass measurement is calculated by propagating the random error of Γ_0 and the error of R (see Supplementary Note 1) using Eq. (4). The random error of Γ_0 is determined from the measurements of $\varphi(f)$ for voltage modulations of 20, 30, and 40 mV (Eq. (3)) as the average error of these three measurements. The measurements at 10 mV are not used for the analysis because of their lower signal-to-noise ratio. The error of R is found by fitting experimental BLS spectra (see below and Supplementary Note 1).

Broad-band light scattering (BLS). The principle of the BLS measurements is described in David et al.³⁰. The output of a fiber-coupled broad-band Xe lamp (Energetiq EQ-99XFC LDLS, spectral range 190–2100 nm) is collimated with a reflective collimator (Thorlabs, RC04FC-F01) and then focused on the particle with a reflective objective (Edmund Optics, 89-722). The elastically scattered light is collected over an angular range of 26.6° centered at a scattering angle of $\theta \approx 37^\circ$ with another identical reflective objective. The collected scattered light is then focused on the fiber of the spectrometer (Andor, Kymera 328i with a Newton A-DU940P-BV camera) with a reflective collimator (Thorlabs, RC04SMA-F01). Two shortpass filters (Edmund optics, 49 825, OD > 4) reduce the signal of the elastic scattering of the trapping laser. The wavelength range $\lambda = 350\text{--}500 \text{ nm}$ is used to retrieve the droplet radius R from fits of the experimental spectra to simulations using Mie theory. R , θ , and n_0 and n_1 of the wavelength-dependent refractive index of the droplet, $n(\lambda)$, are fit parameters. A first order Cauchy parametrization is used for $n(\lambda)$:

$$n(\lambda) = n_0 + n_1 \left(\left(\frac{\lambda_0}{\lambda} \right)^2 - 1 \right) \quad (5)$$

with a reference wavelength of $\lambda_0 = 475 \text{ nm}$. Supplementary Fig. 1 shows representative BLS spectra and the values of R and n_0 determined in this study.

Mass growth factor m^* . In the present experiments, the mass change of a NaCl droplet caused by variation of the RH is purely due to the uptake or loss of water. Hence, the salt mass (m_{NaCl}) in the droplet remains constant. As a cross-check, we determined m_{NaCl} of the trapped droplet at the different constant RHs using the water activity of bulk solutions with known mass fractions⁶⁶. The retrieved values of m_{NaCl} at 78%, 81%, and 86% RH (4.56 ± 0.05 , 4.50 ± 0.02 , and $4.49 \pm 0.02 \cdot 10^{-15} \text{ kg}$, respectively, for one given droplet) agree within 1.5%. Below the critical RH (supersaturated solutions) bulk measurements are not possible so that m_{NaCl} cannot be determined in this way. We thus use the average values of m_{NaCl} determined at 78%, 81%, and 86% RH to calculate the mass growth factor $m^* = m/m_{\text{NaCl}}$ of the droplet for undersaturated and supersaturated solutions (RH = 68%).

Data availability

The data that support the findings of this study are available from the corresponding author upon reasonable request.

Received: 2 September 2020; Accepted: 10 November 2020;

Published online: 04 December 2020

References

- Ashkin, A. Acceleration and trapping of particles by radiation pressure. *Phys. Rev. Lett.* **24**, 156–159 (1970).
- Arita, Y., Mazilu, M. & Dholakia, K. Laser-induced rotation and cooling of a trapped microgyroscope in vacuum. *Nat. Commun.* **4**, 2374 (2013).
- Pérez García, L., Donlucas Pérez, J., Volpe, G., Arzola, A. V. & Volpe, G. High-performance reconstruction of microscopic force fields from Brownian trajectories. *Nat. Commun.* **9**, 5166 (2018).
- McGloin, D. Optical tweezers: 20 years on. *Philos. Trans. R. Soc. Math. Phys. Eng. Sci.* **364**, 3521–3537 (2006).
- He, H., Friese, M. E. J., Heckenberg, N. R. & Rubinsztein-Dunlop, H. Direct observation of transfer of angular momentum to absorptive particles from a laser beam with a phase singularity. *Phys. Rev. Lett.* **75**, 826–829 (1995).
- Maragò, O. M., Jones, P. H., Guicciardi, P. G., Volpe, G. & Ferrari, A. C. Optical trapping and manipulation of nanostructures. *Nat. Nanotechnol.* **8**, 807–819 (2013).
- Dufresne, E. R., Spalding, G. C., Dearing, M. T., Sheets, S. A. & Grier, D. G. Computer-generated holographic optical tweezer arrays. *Rev. Sci. Instr.* **72**, 1810–1816 (2001).
- Liesener, J., Reicherter, M., Haist, T. & Tiziani, H. J. Multi-functional optical tweezers using computer-generated holograms. *Optics Communications* **185**, 77–82 (2000).
- Jesacher, A., Fühapter, S., Bernet, S. & Ritsch-Marte, M. Size selective trapping with optical “cogwheel” tweezers. *Optics Express* **12**, 4129–4135 (2004).
- Ahn, J. et al. Ultrasensitive torque detection with an optically levitated nanorotor. *Nat. Nanotechnol.* **15**, 89–93 (2020).
- Cecconi, C., Shank, E. A., Bustamante, C. & Marqusee, S. Direct observation of the three-state folding of a single protein molecule. *Science* **309**, 2057 (2005).
- Hajizadeh, F. et al. Brownian fluctuations of an optically rotated nanorod. *Optica* **4**, 746–751 (2017).
- Neuman, K. C. & Block, S. M. Optical trapping. *Rev. Sci. Instr.* **75**, 2787–2809 (2004).
- Ashok, P. C. & Dholakia, K. Optical trapping for analytical biotechnology. *Curr. Opin. Biotechnol.* **23**, 16–21 (2012).
- Li, T., Kheifets, S., Medellin, D. & Raizen, M. G. Measurement of the instantaneous velocity of a brownian particle. *Science* **328**, 1673–1675 (2010).
- Reimann, R. et al. GHz rotation of an optically trapped nanoparticle in vacuum. *Phys. Rev. Lett.* **121**, 033602 (2018).
- Svak, V. et al. Transverse spin forces and non-equilibrium particle dynamics in a circularly polarized vacuum optical trap. *Nat. Commun.* **9**, 5453 (2018).
- Wills, J. B., Knox, K. J. & Reid, J. P. Optical control and characterisation of aerosol. *Chem. Phys. Lett.* **481**, 153–165 (2009).
- Gong, Z., Pan, Y.-L., Videen, G. & Wang, C. Optical trapping and manipulation of single particles in air: principles, technical details, and applications. *J. Quant. Spectrosc. Radiat. Transfer* **214**, 94–119 (2018).
- Mitchem, L. & Reid, J. P. Optical manipulation and characterisation of aerosol particles using a single-beam gradient force optical trap. *Chem. Soc. Rev.* **37**, 756–769 (2008).
- Reid, J. P. et al. The viscosity of atmospherically relevant organic particles. *Nat. Commun.* **9**, 956 (2018).
- Cremer, J. W., Thaler, K. M., Haisch, C. & Signorell, R. Photoacoustics of single laser-trapped nanodroplets for the direct observation of nanofocusing in aerosol photokinetics. *Nat. Commun.* **7**, 10941 (2016).
- Cotterell, M. I., Preston, T. C., Orr-Ewing, A. J. & Reid, J. P. Assessing the accuracy of complex refractive index retrievals from single aerosol particle cavity ring-down spectroscopy. *Aerosol Sci. Technol.* **50**, 1077–1095 (2016).
- Davies, J. F. & Wilson, K. R. Raman spectroscopy of isotopic water diffusion in ultraviscous, glassy, and gel states in aerosol by use of optical tweezers. *Anal. Chem.* **88**, 2361–2366 (2016).
- David, G., Esat, K., Thanopoulos, I. & Signorell, R. Digital holography of optically-trapped aerosol particles. *Commun. Chem.* **1**, 46 (2018).
- Davis, R. D., Lance, S., Gordon, J. A. & Tolbert, M. A. Long working-distance optical trap for in situ analysis of contact-induced phase transformations. *Anal. Chem.* **87**, 6186–6194 (2015).
- Cotterell, M. I. et al. Measurements of the evaporation and hygroscopic response of single fine-mode aerosol particles using a Bessel beam optical trap. *Phys. Chem. Chemical Phys.* **16**, 2118–2128 (2014).
- Guillon, M., Dholakia, K. & McGloin, D. Optical trapping and spectral analysis of aerosols with a supercontinuum laser source. *Optics Express* **16**, 7655–7664 (2008).
- Bzdek, B. R., Power, R. M., Simpson, S. H., Reid, J. P. & Royall, C. P. Precise, contactless measurements of the surface tension of picolitre aerosol droplets. *Chem. Sci.* **7**, 274–285 (2016).
- David, G., Esat, K., Ritsch, I. & Signorell, R. Ultraviolet broadband light scattering for optically-trapped submicron-sized aerosol particles. *Phys. Chem. Chemical Phys.* **18**, 5477–5485 (2016).
- King, M. D., Thompson, K. C., Ward, A. D., Pfrang, C. & Hughes, B. R. Oxidation of biogenic and water-soluble compounds in aqueous and organic aerosol droplets by ozone: a kinetic and product analysis approach using laser Raman tweezers. *Faraday Discussions* **137**, 173–192 (2008).
- Athanasias, A. et al. Dynamic viscosity mapping of the oxidation of squalene aerosol particles. *Phys. Chem. Chemical Phys.* **18**, 30385–30393 (2016).
- Davis, E. J. & Ray, A. K. Single aerosol particle size and mass measurements using an electrodynamic balance. *J. Colloid Interface Sci.* **75**, 566–576 (1980).
- Peng, C., Chan, M. N. & Chan, C. K. The hygroscopic properties of dicarboxylic and multifunctional acids: measurements and UNIFAC Predictions. *Environ. Sci. Technol.* **35**, 4495–4501 (2001).
- Tang, I. N., Tridico, A. C. & Fung, K. H. Thermodynamic and optical properties of sea salt aerosols. *J. Geophys. Res. Atmos.* **102**, 23269–23275 (1997).
- Tang, I. N., Fung, K. H., Imre, D. G. & Munkelwitz, H. R. Phase transformation and metastability of hygroscopic microparticles. *Aerosol Sci. Technol.* **23**, 443–453 (1995).
- Davies, J. F. Mass, charge, and radius of droplets in a linear quadrupole electrodynamic balance. *Aerosol Sci. Technol.* **53**, 309–320 (2019).
- Murphy, D. M. Something in the air. *Science* **307**, 1888–1890 (2005).
- Miles, R. E. H., Carruthers, A. E. & Reid, J. P. Novel optical techniques for measurements of light extinction, scattering and absorption by single aerosol particles. *Laser Photon. Rev.* **5**, 534–552 (2011).
- Morris, J. W. et al. Kinetics of submicron oleic acid aerosols with ozone: a novel aerosol mass spectrometric technique. *Geophys. Res. Lett.* **29**, 71–71–4 (2002).
- Smith, G. D., Woods, E., DeForest, C. L., Baer, T. & Miller, R. E. Reactive uptake of ozone by oleic acid aerosol particles: application of single-particle mass spectrometry to heterogeneous reaction kinetics. *J. Phys. Chem. A* **106**, 8085–8095 (2002).
- Bera, S. K. et al. Simultaneous measurement of mass and rotation of trapped absorbing particles in air. *Opt. Lett.* **41**, 4356–4359 (2016).
- Lin, J., Deng, J., Wei, R., Li, Y. Q. & Wang, Y. Measurement of mass by optical forced oscillation of absorbing particles trapped in air. *J. Opt. Soc. Am. B* **34**, 1242–1246 (2017).
- Ashkin, A. & Dziedzic, J. M. Observation of radiation-pressure trapping of particles by alternating light beams. *Phys. Rev. Lett.* **54**, 1245–1248 (1985).
- Constable, A., Kim, J., Mervis, J., Zarinetchi, F. & Prentiss, M. Demonstration of a fiber-optical light-force trap. *Opt. Lett.* **18**, 1867–1869 (1993).
- Čizmar, T., Garcés-Chávez, V., Dholakia, K. & Zemánek, P. Optical conveyor belt for delivery of submicron objects. *Applied Physics Letters* **86**, 174101 (2005).
- Rkhouak, L. et al. Optical trapping and Raman spectroscopy of solid particles. *Phys. Chem. Chem. Phys.* **16**, 11426–11434 (2014).
- Kalume, A., Wang, C., Santarpia, J. & Pan, Y.-L. Study of single airborne particle using laser-trapped submicron position-resolved temporal Raman spectroscopy. *Chem. Phys. Lett.* **706**, 255–260 (2018).
- Rafferty, A., Gorkowski, K., Zuend, A. & Preston, T. C. Optical deformation of single aerosol particles. *Proc. Natl Acad. Sci. USA* **116**, 19880–19886 (2019).
- Esat, K., David, G., Poulkas, T., Shein, M. & Signorell, R. Phase transition dynamics of single optically trapped aqueous potassium carbonate particles. *Phys. Chem. Chemical Phys.* **20**, 11598–11607 (2018).
- Hinds, W. C. *Aerosol Technology: Properties, Behavior, and Measurement of Airborne Particles*. (John Wiley & Sons, 1999).
- Bohren, C. F. & Huffman, D. R. *Absorption and Scattering of Light by Small Particles*. (Wiley, 1983).
- Greenspan, L. Humidity fixed points of binary saturated aqueous solutions. *J. Res. Natl Bureau Stand. Sec. A* **81**, 89–96 (1977).
- Zhang, H.L. & Han, S.J. Viscosity and density of water + sodium chloride + potassium chloride solutions at 298.15 K. *J. Chem. Eng. Data* **41**, 516–520 (1996).
- Topping, D. et al. UManSysProp v1.0: an online and open-source facility for molecular property prediction and atmospheric aerosol calculations. *Geosci. Model Dev.* **9**, 899–914 (2016).
- Zieger, P. et al. Revising the hygroscopicity of inorganic sea salt particles. *Nat. Commun.* **8**, 15883 (2017).
- Zieger, P., Fierz-Schmidhauser, R., Weingartner, E. & Baltensperger, U. Effects of relative humidity on aerosol light scattering: results from different European sites. *Atmos. Chem. Phys.* **13**, 10609–10631 (2013).
- Laskina, O. et al. Size matters in the water uptake and hygroscopic growth of atmospherically relevant multicomponent aerosol particles. *J. Phys. Chem. A* **119**, 4489–4497 (2015).
- Hu, D. et al. Hygroscopicity of inorganic aerosols: size and relative humidity effects on the growth factor. *Aerosol. Air Quality Res.* **10**, 255–264 (2010).
- Swietlicki, E. et al. Hygroscopic properties of submicrometer atmospheric aerosol particles measured with H-TDMA instruments in various environments—a review. *Tellus B* **60**, 432–469 (2008).

61. Park, K. et al. Measurement of adherent cell mass and growth. *Proc. Natl Acad. Sci. USA* **107**, 20691 (2010).
62. Popescu, G., Park, K., Mir, M. & Bashir, R. New technologies for measuring single cell mass. *Lab Chip* **14**, 646–652 (2014).
63. Arlett, J. L., Myers, E. B. & Roukes, M. L. Comparative advantages of mechanical biosensors. *Nat. Nanotechnol.* **6**, 203–215 (2011).
64. Cadart, C., Venkova, L., Recho, P., Lagomarsino, M. C. & Piel, M. The physics of cell-size regulation across timescales. *Nat. Phys.* **15**, 993–1004 (2019).
65. Kalantarifard, F. et al. Intracavity optical trapping of microscopic particles in a ring-cavity fiber laser. *Nat. Commun.* **10**, 2683 (2019).
66. Chirife, J. & Resnik, S. L. Unsaturated solutions of sodium chloride as reference sources of water activity at various temperatures. *J. Food Sci.* **49**, 1486–1488 (1984).

Acknowledgements

This work was supported by the Swiss National Science Foundation (SNSF grant no. 200020_172472) and ETH Zurich. We would like to thank David Stapfer and Markus Steger from the ETH mechanical and electronic shop for their help. We would like to acknowledge the contributions of Johannes Cremer in the early stage of this project.

Author contributions

R.S. conceived the project. R.S. and G.D. supervised the project. G.D., O.R., and K.E. implemented the experimental set-up. O.R. performed the experiments and the analysis of the experimental data with assistance from G.D. O.R., G.D., and R.S. wrote the paper. All authors discussed the results and the manuscript.

Competing interests

The authors declare no competing interests.

Additional information

Supplementary information is available for this paper at <https://doi.org/10.1038/s42005-020-00496-x>.

Correspondence and requests for materials should be addressed to G.D. or R.S.

Reprints and permission information is available at <http://www.nature.com/reprints>

Publisher's note Springer Nature remains neutral with regard to jurisdictional claims in published maps and institutional affiliations.



Open Access This article is licensed under a Creative Commons Attribution 4.0 International License, which permits use, sharing, adaptation, distribution and reproduction in any medium or format, as long as you give appropriate credit to the original author(s) and the source, provide a link to the Creative Commons license, and indicate if changes were made. The images or other third party material in this article are included in the article's Creative Commons license, unless indicated otherwise in a credit line to the material. If material is not included in the article's Creative Commons license and your intended use is not permitted by statutory regulation or exceeds the permitted use, you will need to obtain permission directly from the copyright holder. To view a copy of this license, visit <http://creativecommons.org/licenses/by/4.0/>.

© The Author(s) 2020